Available online at www.sciencedirect.com

ScienceDirect

Geochimica et Cosmochimica Acta 307 (2021) 72–85

Geochimica et Cosmochimica Acta

www.elsevier.com/locate/gca

The nature and origin of upper mantle heterogeneity beneath the Mid-Atlantic Ridge 33–35°N: A Sr-Nd-Hf isotopic perspective

Pengyuan Guo [a,b,*], Yaoling Niu [a,b,c,d], Pu Sun [a,b], Junjie Zhang [a,b], Shuo Chen [a,b], Meng Duan [a,b], Hongmei Gong [a,b], Xiaohong Wang [a,b]

[a] *Key Laboratory of Marine Geology and Environment, Institute of Oceanology, Chinese Academy of Sciences, Qingdao 266071, China*
[b] *Qingdao National Laboratory for Marine Science and Technology, Qingdao 266061, China*
[c] *Department of Earth Sciences, Durham University, Durham DH1 3LE, UK*
[d] *School of Earth Science and Resources, China University of Geosciences, Beijing 100083, China*

Received 6 May 2020; accepted in revised form 17 May 2021; available online 23 May 2021

Abstract

We present new Sr-Nd-Hf isotopic data on mid-ocean ridge basalts from two ridge segments (OH-1, OH-3) between the Oceanographer and Hayes fracture zones at the Mid-Atlantic Ridge 33–35°N to constrain the nature and origin of upper mantle heterogeneity beneath the Mid-Atlantic Ridge. Together with the major and trace elements data (Niu et al., 2001), the new Sr-Nd-Hf isotopic data illustrate that the mantle sources of these lavas comprise three components, i.e., a depleted mantle with high radiogenic Hf isotopic compositions (ADM), an incompatible elemental enriched component with radiogenic Sr and un-radiogenic Nd-Hf isotopic compositions (E-type I), and an incompatible element depleted component with variably enriched Sr-Nd-Hf isotope compositions (i.e., E-type II). The ADM and E-type I components may be understood as representing ancient mantle melting residues and metasomatic veins developed at the base of the thickening oceanic lithosphere, respectively. The unique E-type II component is best explained as recent mantle melting residues of a geochemically enriched mantle, probably associated with the Azores mantle plume to the north. Taking together, we interpret the E-MORB dominated OH-1 lavas as resulting from a relatively higher degree melting of a mantle source composed of ADM matrix and E-type I material, whereas the N-MORB dominated OH-3 lavas resulting from lower degree melting of the mantle source primarily comprising ADM and E-type II components. Such a petrological and geochemical understanding explains the contrast in crustal thickness, ridge morphology and tomography, and mantle Bouguer anomalies between the two ridge segments.

Keywords: Mid-Atlantic Ridge; Mid-ocean ridge basalt; Sr-Nd-Hf isotopes; Upper mantle heterogeneity; Mantle endmembers

1. INTRODUCTION

Mid-ocean ridge basalts (MORB) are traditionally considered to be the simplest igneous rock on earth due to their relatively uniform geochemical compositions (vs. intraplate ocean island and island arc basalts). However, MORB compositional variations have been well documented on all scales (see Niu, 2016 for review) and range in composition from incompatible element depleted normal MORB (i.e., N-MORB) to incompatible element enriched E-type MORB (i.e., E-MORB). The cause of MORB source heterogeneity has been the focus of research for decades and the debate continues to this day concerning the origin of the enriched heterogeneities. Many researchers explain the E-MORB source to be the upper mantle contaminated

* Corresponding author at: Institute of Oceanology, Chinese Academy of Sciences, Nanhai Road 7, Qingdao, Shandong 266071, China.
E-mail address: guopy@qdio.ac.cn (P. Guo).

https://doi.org/10.1016/j.gca.2021.05.033
0016-7037/

by mantle plume materials (e.g., Sun and Hanson, 1975; Schilling et al., 1983; Douglass et al., 1999; Le Roux et al., 2002; Andres et al., 2002), but the enriched heterogeneities could also be generated within the upper mantle without mantle plume influence as evidenced by production of E-MORB from ridges far from any mantle plumes (e.g., Zindler et al., 1984; Niu et al., 1996, 2001, 2002; Donnelly et al., 2004; Waters et al., 2011; Ulrich et al., 2012). To test these ideas, we choose to carry out a Sr-Nd-Hf isotopic study on a unique MORB sample suite from two ridge segments, OH-1 and OH-3, between the Oceanographer and Hayes fracture zones at the Mid-Atlantic Ridge (MAR) 33–35°N (Fig. 1). Furthermore, given the same spreading rate of the two segments only ~90 km apart (DeMets et al., 1990) and thus similar mantle potential temperature, the contrasting petrological (MORB major and trace element compositions) and ridge geological characteristics led Niu et al. (2001) to conclude that mantle source compositional difference controls the extent of mantle melting, crustal production, gravity anomaly, ridge morphology and ridge segmentation between the two ridge segments. While these conclusions are robust in terms of the contrasted magmatism, it is essential to understand the nature and origin of these mantle compositional heterogeneities.

Here we present the results of our systematic Sr-Nd-Hf isotopic study on MORB samples from segments OH-1 and OH-3, Mid-Atlantic Ridge (MAR) 33–35°N (Fig. 1). We identified three mantle components beneath the MAR: a depleted component with high radiogenic Hf isotope (ADM), an enriched component in terms of Sr-Nd-Hf isotopes and incompatible elements (E-type I), and an incompatible element depleted but isotopically enriched component (E-type II). While the ADM and E-type I are most consistent, respectively, with ancient peridotitic melting residue and ancient metasomatic vein lithologies created in oceanic lithosphere environments, the E-type II is best understood as representing recent melting residue of the Azores mantle plume with caveats. We infer that the mantle source beneath this part of the MAR is dominated by ADM with abundant E-type I material beneath OH-1, and abundant E-type II material beneath OH-3. We present our perspectives on the development of these mantle source heterogeneities with emphasis on the contrast between segments OH-1 and OH-3.

2. GEOLOGICAL BACKGROUND AND SAMPLES

Many seagoing expeditions have been carried out at the Mid-Atlantic Ridge 33–35°N (Fig. 1a) between the Hayes fracture zone (FZ) and Oceanographer FZ because the ridge segments have distinctive and contrasting topography, morphology and gravity anomalies (e.g., Schilling, 1975; Detrick et al., 1995; Dosso et al., 1999; Bideau et al., 1998; Gràcia et al., 1999). These expeditions collected detailed bathymetric, gravity and seismic data and carried out intensive sampling along the ridge and nearby seamounts. Briefly, the MAR between the Oceanographer FZ and Hayes FZ can be divided into five segments separated by non-transform discontinuities. The segments are numbered OH-1 to OH-5 (Detrick et al., 1995), going southwards from the Oceanographer FZ to the Hayes FZ (Fig. 1b). Segment OH-1 is characterized by an axial high, a greater length (~90 km), a shallow central topography high (1700–2000 m at ridge), a large negative mantle

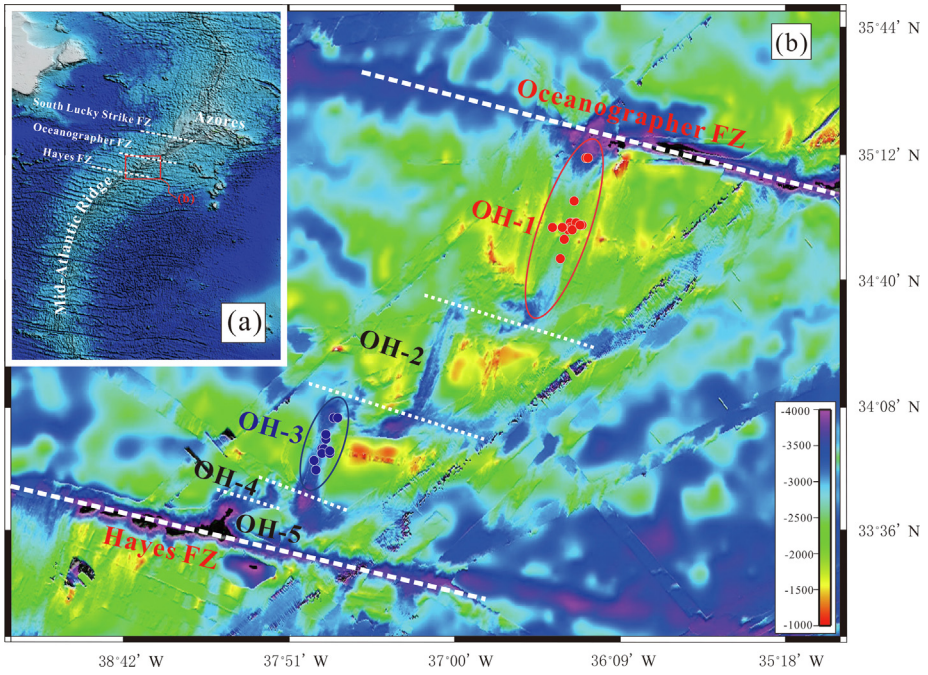

Fig. 1. (a) Portion of the bathymetric map of the North Atlantic. (b) Detailed bathymetric map showing the Mid-Atlantic Ridge between the Oceanographer Fracture Zone (OFZ) and the Hayes Fracture Zone (HFZ) (data from NOAA bathymetric coverage). Sample locations are shown as red (segment OH-1) and blue (segment OH-3) filled circles.

Bouguer anomaly (~40 mGal) of bull's eye shape and an inferred thicker crust with robust magmatism (Detrick et al., 1995; Bideau et al., 1998; Gràcia et al., 1999). In contrast, segment OH-3 has a shorter segment (~45 km), a deep axial valley (3000–3500 m), smaller mantle Bouguer anomaly (<20 mGal) and thin crust (Detrick et al., 1995; Bideau et al., 1998; Gràcia et al., 1999).

Samples in this study from segment OH-1 and OH-3 (Fig. 1b) were collected using submersible OCEANAUT aboard R/V Nadir. These samples are fresh basalts and some are fresh glasses (Bideau et al., 1998; Niu et al., 2001). Abundant analyses of bulk rock major and trace elements on these samples show that the OH-3 lavas are mainly N-MORB ($[La/Sm]_N < 1$) and the OH-1 samples are dominated by variably enriched E-MORB ($[La/Sm]_N > 1$) (Niu et al., 2001).

3. ANALYTICAL TECHNIQUES

Major elements on 27 samples and trace elements on 99 samples from OH-1 and OH-3 segments were previously reported in Niu et al. (2001). Eighteen OH-1 samples and 14 OH-3 samples that encompass the entire OH-1 and OH-3 lavas compositional spectrum defined by trace elements were analyzed for bulk rock Sr-Nd-Hf isotopes (Table 1). Some of our samples are rock powders and some are glass fragments. For glass fragments, samples were handpicked under a binocular to avoid alteration and phenocrysts (olivine and plagioclase). Before digestion for isotope analyses, sample fragments were ultrasonically cleaned in Milli-Q water. All the analytical work was done in the Laboratory of Ocean Lithosphere and Mantle Dynamics, Institute of Oceanology, Chinese Academy of Sciences.

About 50–100 mg dried (powder or fragment) material for each sample was weighted to analyze Sr-Nd-Hf isotopes. The digestion and Sr-Nd-Hf purification follow the procedures given in Chen et al. (2017) and Sun et al. (2019), respectively. The isotope analyses were all conducted using a Nu Plasma II Multi-Collector Inductively Coupled Plasma Mass Spectrometer (MC-ICP-MS). The measured $^{87}Sr/^{86}Sr$, $^{143}Nd/^{144}Nd$ and $^{176}Hf/^{177}Hf$ isotope ratios were normalized for instrumental mass bias fractionation using the exponential law to $^{86}Sr/^{88}Sr = 0.1194$, $^{146}Nd/^{144}Nd = 0.7219$ and $^{179}Hf/^{177}Hf = 0.7325$, respectively. Repeated analyses of NBS-987 standard gave $^{87}Sr/^{86}Sr = 0.710259 \pm 18$ (N = 12, 2σ), JNdi-1 standard gave $^{143}Nd/^{144}Nd = 0.512118 \pm 9$ (N = 8, 2σ) and Alfa Hf standard gave $^{176}Hf/^{177}Hf = 0.282187 \pm 8$ (N = 8, 2σ) in the course of our sample analyses. The analytical data are given in Table 1. The isotopic analyses of the USGS reference materials BHVO-2, BCR-2 and AGV-2 (Table 1) run together with our samples agree well with the reported values (GeoREM, http://georem.mpch-mainz.gwdg.de/).

In addition, new major elements for 5 samples were also analyzed using Agilent 5100 Inductively Coupled Plasma Optical Emission Spectrometer (ICP-OES) and is presented in Table S1. The bulk-rock major elements of the USGS reference materials BCR-2 and AGV-2 (Table S1) analyzed together with our samples agree well with reference values within error.

4. RESULTS

The Sr-Nd-Hf isotopic data on OH-1 lavas confirm the previous report on samples from the same segment (Dosso et al., 1999; Debaille et al., 2006; also see Fig. 2). These samples, like other MORB from the Mid-Atlantic Ridge at 33–40°N, display good correlations in ε_{Hf}–$^{87}Sr/^{86}Sr$ and ε_{Hf}–ε_{Nd} spaces, but define their trends deviate from the global MORB trend (or mantle array) with steeper slopes (Fig. 3). Compared with OH-1 samples, the OH-3 samples show similar ranges in $^{87}Sr/^{86}Sr$ and ε_{Hf} variation ranges but have a slightly smaller range in ε_{Nd} (Fig. 2). The OH-3 samples can be further divided into two groups according to their Hf isotopic compositions (Figs. 2 and 3): (1) Group-1, samples are isotopically homogeneous and depleted with low $^{87}Sr/^{86}Sr$ and high ε_{Nd}, ε_{Hf}; (2) Group-2, samples are less depleted or slightly enriched for ε_{Nd} and ε_{Hf} but varied (lowest to highest) $^{87}Sr/^{86}Sr$. Samples with the Group-2 signature have not been observed previously (Dosso et al., 1999; Debaille et al., 2006), and show decoupling in ε_{Hf}–$^{87}Sr/^{86}Sr$ space (Fig. 3). Fig. 4 shows along-axis variation of Sr-Nd-Hf isotopic ratios of these samples. It is obvious that the lavas with higher $^{87}Sr/^{86}Sr$ and low ε_{Nd}, ε_{Hf} occupy the center of OH-1 segment with the most isotopic enrichment coinciding with the central topographic high, which is consistent with incompatible element enrichments (see Fig. 3 in Niu et al., 2001). However, this is not the case for OH-3 segment, which is also consistent with incompatible element distribution (Niu et al., 2001). Fig. 5 illustrates the Sr-Nd-Hf isotope variations as a function of Ba and $[La/Sm]_N$ in OH-1 and OH-3 lavas. The majority of OH-1 samples (excluding three incompatible element depleted N-MORB samples OT16-11, OT18-11 and OT19-04) and three E-MORB lavas from OH-3 segment (encircled with blue dotted lines in Fig. 5) show good correlations between Sr-Nd-Hf isotopes and these geochemical parameters, but the other OH-3 N-MORB samples do not.

5. DISCUSSION

5.1. Nature and origin of the OH-1 lava mantle source

Apart from the three incompatible element depleted N-MORB samples (OT16-11, OT18-11 and OT19-04), the majority of OH-1 samples show well correlated relationships between Sr-Nd-Hf isotopes and Ba and $[La/Sm]_N$ (Fig. 5). These correlations can be explained as the result of melting-induced mixing of two mantle component mantle source, i.e., melting to varying extents of such composite components or melting to similar extents of a mantle containing variable proportions of the two components (Niu et al., 1999, 2002; Koornneef et al., 2012), as is exampled by the near-ridge seamount lavas from the East Pacific Rise (Niu et al., 2002; Zhang et al., 2016) and MORB lavas from the Pacific-Antarctic Ridge (Castillo et al., 1998). One endmember is the depleted mantle with low incompatible

Table 1
Sr-Nd-Hf isotopic analysis results on MORB lavas from MAR 33-35° N and USGS materials.

Sample	Segment	Site	Lat. (°N)	Long. (°N)	Dbsl (m)	$^{87}Sr/^{86}Sr$	2s.e.	$^{143}Nd/^{144}Nd$	2s.e.	$^{176}Hf/^{177}Hf$	2s.e.	ε_{Nd}	ε_{Hf}
OT01-04	OH-1	Axis	34.8937	−36.4280	2228	0.702855	15	0.513157	9	0.283323	3	10.1	19.5
OT01-07	OH-1	Axis	34.8945	−36.4355	2230	0.702892	14	0.513161	11	0.283319	4	10.2	19.4
OT02-09	OH-1	Axis	34.8670	−36.4382	2252	0.702887	11	0.513145	9	0.283322	4	9.9	19.4
OT02-11	OH-1	Axis	34.8603	−36.4333	2225	0.703209	8	0.512990	9	0.283139	6	6.9	13.0
OT03-02	OH-1	Axis	34.8230	−36.4675	2331	0.703017	11	0.513060	9	0.283259	11	8.2	17.2
OT05-02	OH-1	Off-Axis	34.8900	−36.4143	2200	0.702983	12	0.513107	7	0.283280	3	9.1	18.0
OT05-08	OH-1	Off-Axis	34.8845	−36.3882	1718	0.703275	6	0.512942	6	0.283129	4	5.9	12.6
OT05-08R						0.703283	7	0.512937	8	0.283132	6	5.8	12.7
OT05-13	OH-1	Off-Axis	34.8783	−36.3763	1438	0.703394	9	0.512969	9	0.283129	5	6.5	12.6
OT06-01	OH-1	Off-Axis	34.8800	−36.3800	1991	0.703254	7	0.513001	7	0.283122	32	7.1	12.4
OT16-01	OH-1	Off-Axis	34.8718	−36.5305	2075	0.703060	10	0.513124	8	0.283292	4	9.5	18.4
OT16-11	OH-1	Axis	34.8717	−36.4755	1688	0.703230	7	0.513086	13	0.283187	6	8.7	14.7
OT16-11R						0.703238	7	0.513083	7	0.283187	7	8.7	14.7
OT17-06	OH-1	Axis	34.9773	−36.4203	2332	0.703140	11	0.513059	8	0.283242	4	8.2	16.6
OT17-09	OH-1	Axis	34.9795	−36.4185	2460	0.703208	12	0.513067	9	0.283274	4	8.4	17.8
OT18-04	OH-1	Axis	34.8648	−36.4500	1976	0.703206	12	0.512991	7	0.283151	4	6.9	13.4
OT18-11	OH-1	Axis	34.8730	−36.4683	1652	0.703060	6	0.513077	9	0.283256	120	8.6	17.1
OT19-04	OH-1	Axis	34.7378	−36.4923	2677	0.702867	13	0.513147	12	0.283272	5	9.9	17.7
OT20-05	OH-1	Axis	35.1647	−36.3613	3477	0.703007	12	0.513106	6	0.283307	5	9.1	18.9
OT20-06	OH-1	Axis	35.1587	−36.3460	3340	0.702981	12	0.513129	10	0.283332	5	9.6	19.8
OT09-05	OH-3	Axis	33.9420	−37.6950	3075	0.702837	11	0.513074	11	0.283144	4	8.5	13.2
OT09-06	OH-3	Axis	33.9377	−37.6943	3060	0.702820	12	0.513067	9	0.283146	6	8.4	13.2
OT09-12	OH-3	Axis	33.9205	−37.6967	3083	0.702851	11	0.513075	10	0.283090	4	8.5	11.2
OT10-06	OH-3	Axis	33.9835	−37.6773	3173	0.702936	13	0.513122	10	0.283291	5	9.4	18.4
OT10-06R						0.702955	15	0.513126	11	0.283294	5	9.5	18.4
OT10-11	OH-3	Axis	33.9963	−37.6762	3226	0.702926	13	0.513133	10	0.283319	5	9.7	19.4
OT11-10	OH-3	Axis	33.8458	−37.7307	3283	0.702959	12	0.513116	12	0.283327	7	9.3	19.6
OT11-12	OH-3	Axis	33.8470	−37.7297	3183	0.702963	13	0.513118	9	0.283312	5	9.4	19.1
OT12-03	OH-3	Axis	33.9265	−37.6642	2961	0.703054	12	0.513062	8	0.283204	6	8.3	15.3
OT12-05	OH-3	Axis	33.9228	−37.6567	2900	0.702932	12	0.513168	10	0.283326	5	10.3	19.6
OT13-05	OH-3	Axis	33.8877	−37.7380	3114	0.702969	9	0.513112	11	0.283307	5	9.2	18.9
OT13-07	OH-3	Axis	33.8877	−37.7383	3048	0.702947	12	0.513115	9	0.283302	4	9.3	18.7
OT14-01	OH-3	Axis	34.0698	−37.6363	3562	0.703161	11	0.513033	10	0.283181	6	7.7	14.5
OT14-02	OH-3	Axis	34.0697	−37.6360	3561	0.703369	12	0.513046	12	0.283184	6	8.0	14.6
OT14-04	OH-3	Axis	34.0688	−37.6213	3352	0.702943	12	0.513142	10	0.283334	4	9.8	19.9
BHVO-2						0.703473	12	0.512987	8	0.283087	4		
BCR-2						0.705043	12	0.512637	8	0.282854	4		
AGV-2						0.704005	10	0.512777	10	0.282956	11		

Note: ε_{Nd} and ε_{Hf} are calculated as parts per 10^4 relative deviation of measured $^{143}Nd/^{144}Nd$ and $^{176}Hf/^{177}Hf$ from present-day chondritic reservoirs, namely $^{143}Nd/^{144}Nd = 0.512638$ (Jacobsen and Wasserburg, 1980) and $^{176}Hf/^{177}Hf = 0.282772$ (Blichert-Toft and Albarede, 1997). Dbsl-depth below sea level. Several repeated analysis are denoted as R.

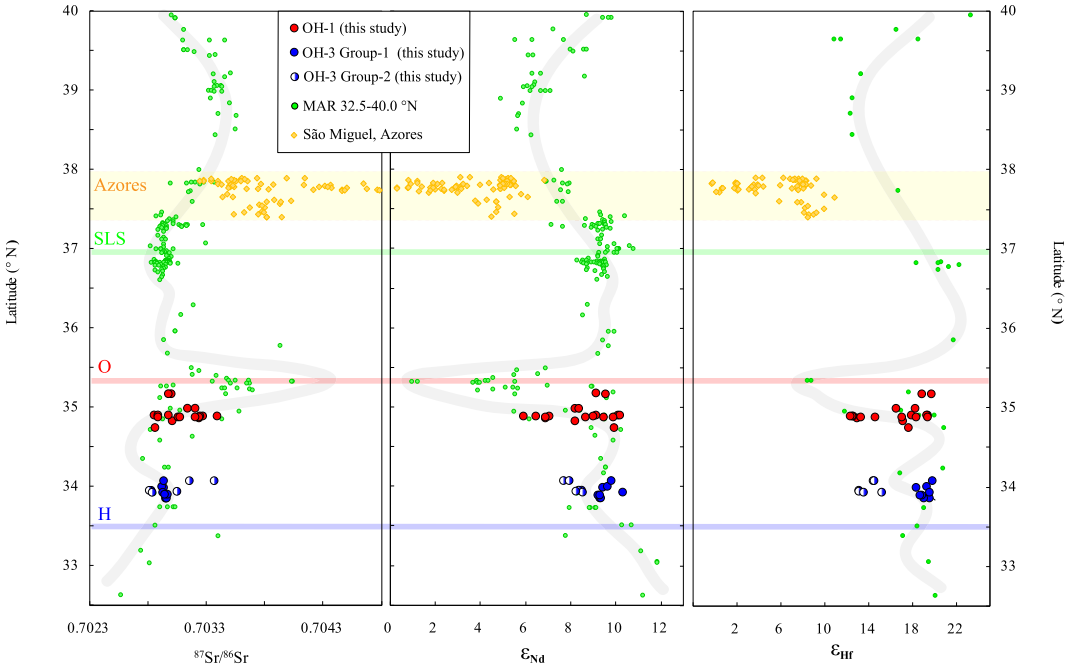

Fig. 2. $^{87}Sr/^{86}Sr$, ε_{Nd} and ε_{Hf} of MAR MORBs as a function of latitude (32.5–40°N). From north to south SLS, O and H stand for South Lucky Strike, Oceanographer and Hayes fracture zones. Reference isotopic data of the samples from MAR 32.5 to 40°N are from PetDB (www.earthchem.org/petdb), and the São Miguel basalts data are from Elliott et al (2007), Beier et al. (2007) and Waters et al. (2020).

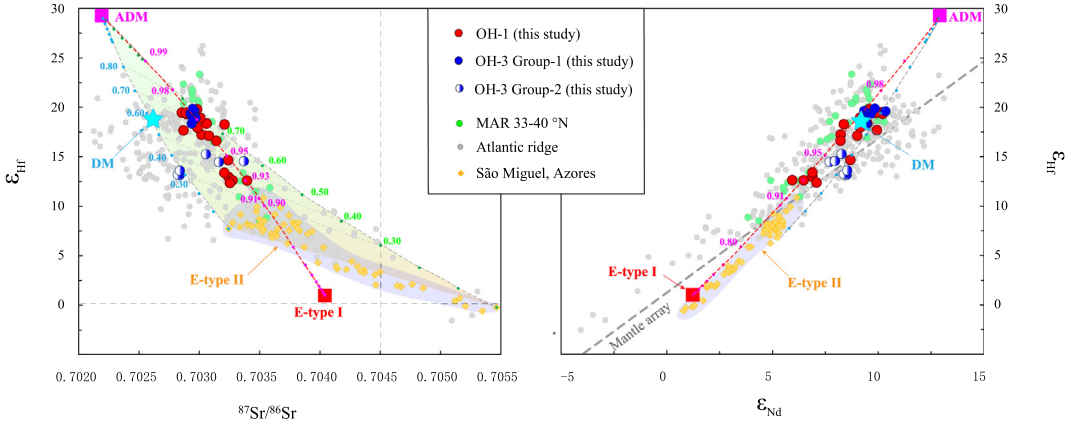

Fig. 3. (a) ε_{Hf} versus $^{87}Sr/^{86}Sr$ and (b) ε_{Hf} versus ε_{Nd} plots to compare the OH-1 and OH-3 lavas with MORB data from MAR 33.5–40°N and from the whole Mid-Atlantic Ridge (data from PetDB: www.earthchem.org/petdb). The red dashed line indicates the two-endmember mixing modelling, in which OH-1 lavas plot along the mixing curve between ADM and E-type I. Also shown is the region (grey dashed line) defined by mixing between ADM and varying mantle plume residue compositions (Elliott et al., 2007; Beier et al., 2007; Waters et al., 2020), and the Group-2 OH-3 lavas are all plotted in the fields enclosed by the, grey dashed lines. The Sr, Nd, Hf concentrations and $^{87}Sr/^{86}Sr$, $^{143}Nd/^{144}Nd$, $^{176}Hf/^{177}Hf$ of the ADM, E-type I and E-type II endmembers in the modeling are given in Table S3. DM denotes the average MORB (Salters and Stracke, 2004).

element (e.g., Ba) concentrations, low $[La/Sm]_N$, low $^{87}Sr/^{86}Sr$, but high ε_{Nd} and high ε_{Hf} (Fig. 5; Table 2). In the case of the OH-1 MORB lavas, this depleted mantle component displays higher ε_{Hf} at a given $^{87}Sr/^{86}Sr$ and ε_{Nd} than the commonly perceived depleted MORB mantle (DM; Salters and Stracke, 2004) in the Hf-Sr and Hf-Nd isotopic plots (Fig. 3). Fig. 3 also shows that our OH-1 samples, together with the MORB literature data from the MAR 33–40°N, form trends with steeper slopes that deviate from the mantle array, implying that all these MAR MORB lavas shared a similarly depleted mantle, which is supposed to be different from the Pacific mantle in term of Hf isotopic compositions (Salters et al., 2011). It has been proposed that this observation is caused by disequilibrium melting of a source of which there is isotopic disequilibrium on mineral grain scales (Blichert-Toft et al., 2005). However, experimental study on diffusion of REEs in garnet demonstrates that centimeter-scale

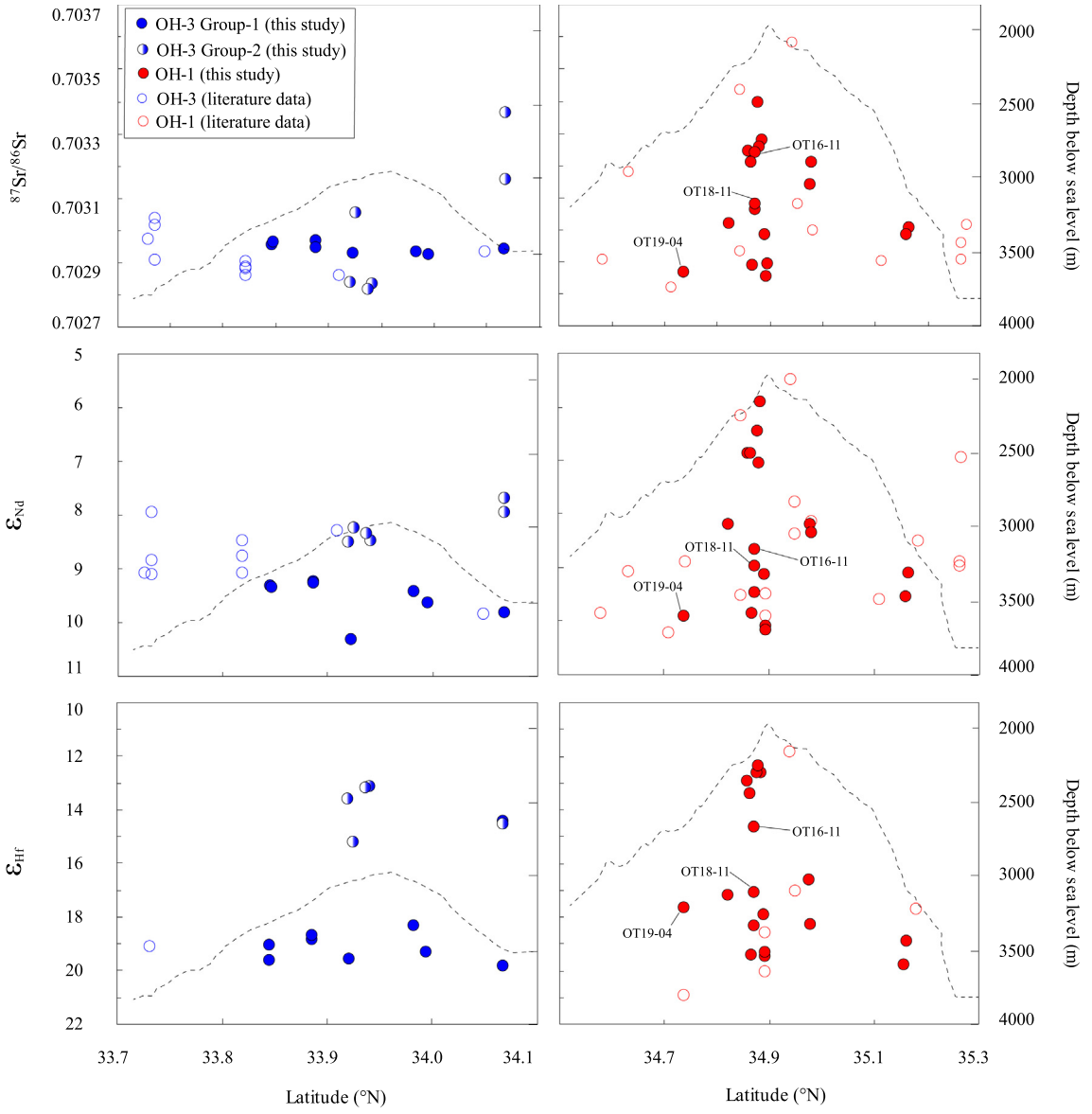

Fig. 4. $^{87}Sr/^{86}Sr$, ε_{Nd} and ε_{Hf} on OH-1 and OH-3 lavas plotted along the ridge axis. The literature data are from PetDB (www.earthchem.org/petdb). The dashed lines are along-ridge bathymetry (Detrick et al., 1995). Note that the ε_{Nd} and ε_{Hf} scales are inverted.

equilibration at peridotite solidus temperatures requires a time scale of 1–2 million years (Van Orman et al., 2002). Some others explained this unique mantle component as originating from involvement of an ancient melting residue in the presence of garnet (e.g., Hamelin et al., 2013; Salters et al., 2011). This is because Lu is compatible in garnet and such residue will have high Lu/Hf to produce, with enough time, high $^{176}Hf/^{177}Hf$. In contrast to the Lu–Hf system, Sm and Nd show less fractionation in minerals of garnet and spinel peridotites and are more equally affected by the two different melting regimes. Rb is more incompatible than Sr in both garnet and spinel peridotite stability fields and partial melting residues will have too low Rb/Sr to produce high $^{87}Sr/^{86}Sr$. We prefer this explanation in this study. Because this unique depleted component with higher ε_{Hf} at a given ε_{Nd} and $^{87}Sr/^{86}Sr$ (hereafter termed as ADM) is also observed in MORB lavas from the Lucky Strike segment at the 37.3°N MAR (Hamelin et al., 2013) and the southern MAR from 7.5 to 11.5°S (Paulick et al., 2010), it is thus possible that the ADM is commonly distributed beneath the whole MAR.

With the ADM serving as the depleted endmember in the mantle source of the OH-1 lavas, the enriched component, here termed as enriched-type I (E-type I), is characterized by the elevated incompatible element concentrations, high $[La/Sm]_N$, radiogenic Sr and un-radiogenic Nd-Hf isotopic compositions (Fig. 5 and Table 2). Shirey et al. (1987) first reported the highly enriched Sr-Nd-Pb isotopic compositions in MAR MORB from the Oceanographer FZ and nearby seamounts. Such remarkably enriched lavas from the same sampling area were also observed by Dosso et al. (1999), and later supplemented with Hf isotope data

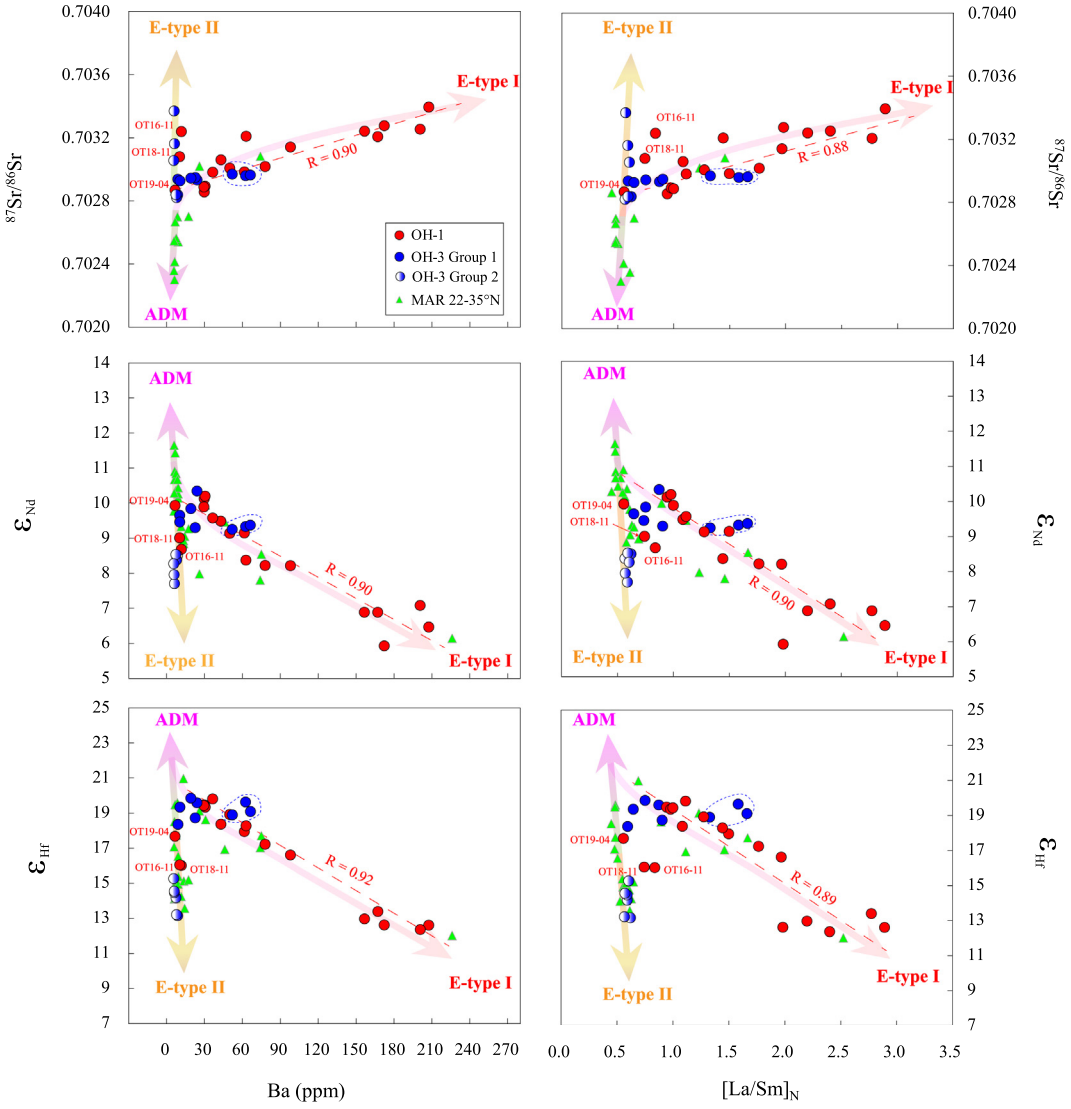

Fig. 5. $^{87}Sr/^{86}Sr$, ε_{Nd} and ε_{Hf} variations of OH-1 and OH-3 lavas as a function of highly incompatible elements such as Ba and highly-to-moderately incompatible element ratios such as $[La/Sm]_N$. Subscript N denotes primitive mantle normalized (Sun and McDonough, 1989). The three less depleted samples (OT11-10, OT11-12 and OT13-05) from OH-3 segment are encircled with blue dotted lines. The correlation coefficient R for the OH-1 samples is calculated excluding three incompatible element depleted samples OT16-11, OT18-11 and OT19-04, which are considered as a whole together with Group-2 OH-3 samples. Red arrows indicate mixing between ADM and E-type I components, and yellow arrows indicate mixing between ADM and E-type II components. Nd-Hf isotopic data of MAR 22–35°N MORB are from Debaille et al. (2006), and Sr isotopic data of these samples are compiled from PetDB (www.earthchem.org/petdb).

by Debaille et al. (2006), though these authors used different samples. These special lavas from the Oceanographer FZ are the most enriched MORB samples thus far reported along the MAR (Fig. 2), and can be considered as the best proxy for the enriched isotopic compositions of the MAR E-type I component.

Following the above, we choose the most enriched sample (AII127–D44GL; Dosso et al. 1999) with highest $^{87}Sr/^{86}Sr$ and lowest ε_{Nd} from the Oceanographer FZ to approximate the E-type I isotopic component. As this sample has no Hf isotope analysis, we can approximate its $^{176}Hf/^{177}Hf$ value using $^{143}Nd/^{144}Nd$ of sample AII127–D44GL from MAR 33–40°N (Dosso et al. 1999) in Sr-Hf and Nd-Hf isotopic plots (Fig. 3). Because the actual depleted component must be more depleted than the most depleted lavas, we infer its $^{176}Hf/^{177}Hf = 0.2836$ along the $^{87}Sr/^{86}Sr$-ε_{Hf} trend of the samples from OH-1 segment and MAR 33–40°N to $^{87}Sr/^{86}Sr = 0.7022$ to approximate the isotopic compositions of this unique endmember. We also model the Sr, Nd, Hf elemental compositions using two-step melting method (see Table S4 for details). Despite the composition of these two endmembers are not unique (see Table S3), our modelling conceptually indicates that OH-1 samples can be explained as resulting from melting-induced mixing between 98–91% ADM and 2–9% E-type I (see Fig. 3).

Fig. 6 shows the correlated variations of Sr–Nd–Hf isotopic ratios with incompatible element abundances and the

Table 2
Geochemical characteristics of the inferred ADM, E-type I and E-type II components beneath the MAR 33–35°N.

	Representative	ADM component	E-type I component	E-type II component
Incompatible element	P_2O_5, K_2O, Ba, Th, Nb	Low	High	Low
Incompatible element ratio	$[La/Sm]_N$, K_2O/TiO_2, Nb/Zr, Zr/Y	Low	High	Low
Radiogenic isotopes	$^{87}Sr/^{86}Sr$	Low	High	Variably high
	$^{143}Nd/^{144}Nd$	High	Low	Variably low
	$^{176}Hf/^{177}Hf$	Extremely high	Low	Variably low
Origin		Recycled melting residues of oceanic lithospheric mantle	Recycled metasomatic veins formed at the base of oceanic lithosphere	Azores mantle plume melting residues

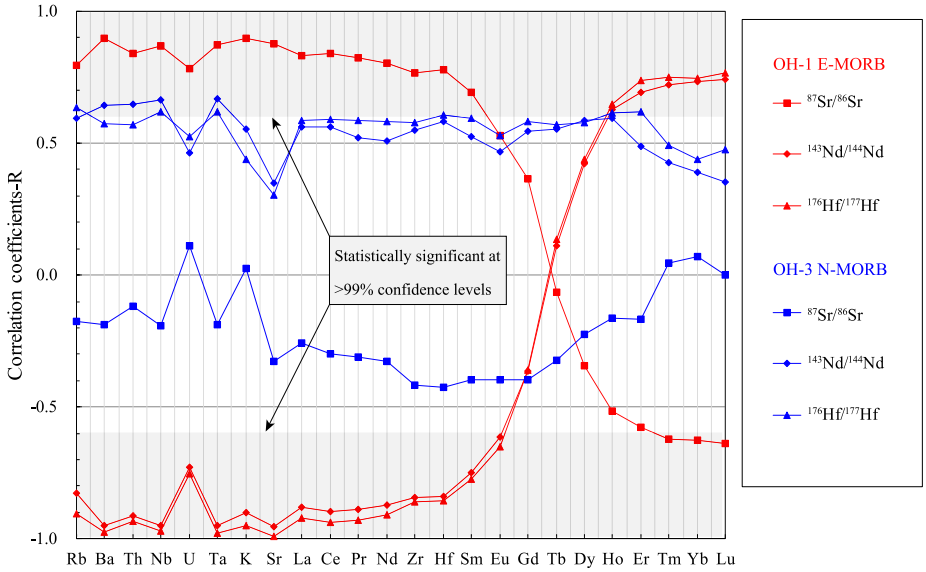

Fig. 6. Correlation coefficients (R-values; left axis) of Sr–Nd–Hf isotopic ratios with incompatible element abundances of OH-1 and OH-3 lavas. The incompatible elements are plotted in the order of decreasing relative incompatibility from left to right. The significant coupling between Sr-Nd-Hf isotopic ratios and incompatible element abundances in OH-1 E-MORB samples demonstrates the ancient nature of both the DM and EI components. The decoupled correlations of Sr–Nd–Hf isotopic ratios with incompatible element abundances in OH-3 N-MORB lavas is consistent with the E-type II component having experienced recent melts extraction. In the plot, the correlation coefficient R for the OH-1 E-MORB is calculated excluding three incompatible element depleted samples OT16-11, OT18-11 and OT19-04, and the correlations coefficient R for the OH-3 N-MORB is calculated excluding three less depleted samples (OT11-10, OT11-12 and OT13-05) encircled with blue dotted lines in Fig. 5.

correlation coefficients increase for the progressively more incompatible elements in OH-1 E-MORB lavas. This observation, together with the correlated variations between radiogenic isotopes and incompatible element ratios (Fig. 5) and among radiogenic isotopes (Fig. 3) in OH-1 samples, indicates explicitly that the two endmembers both must have been of magmatic origin, must be ancient and must have developed their isotopic systematics independently for at least 1.0 Gyrs. This is because (1) magmatism determines the relative abundances of incompatible elements in the melt (e.g., high Rb/Sr, low Sm/Nd and low Lu/Hf) and in the residue (e.g., low Rb/Sr, high Sm/Nd and high Lu/Hf) with respect to the source rock prior to the melting; (2) radiogenic isotope production is a function of the ratio of radioactive parent and radiogenic daughter (i.e., P/D = Rb/Sr, Sm/Nd and Lu/Hf) and also requires time (t), i.e., $^{87}Sr/^{86}Sr = f(t, [^{87}Rb/^{86}Sr])$, $^{143}Nd/^{144}Nd = f(t, [^{147}Sm/^{143}Nd])$ and $^{176}Hf/^{177}Hf = f(t, [^{176}Lu/^{177}Hf])$. Therefore, patrial melting of such two-component mantle will give rise to the observed coupling between incompatible elements and radiogenic isotopes (Mahoney et al., 1994), the melting induced mixing in geochemical plots such as Fig. 5 and the observed correlations manifested in Fig. 6 (also see Niu et al., 2002).

We should also note that the correlation coefficient switch over at about Gd and Tb with the correlations becoming better for the progressively heavier rare earth elements (i.e., from Tb to Lu; Fig. 6), indicating that the enriched E-type I component must have developed in the depth of garnet peridotite stability field in its history. All

these observations and reasoning provide insights into the origin of the incompatible element enriched component in the E-MORB mantle source.

Current models on the origin of the E-MORB enriched mantle source include: recycled metasomatized mantle lithosphere materials (e.g., Niu et al., 2002, 2012; Niu and O'Hara, 2003; Donnelly et al., 2004), recycled ocean crust (e.g., Hirschmann and Stolper, 1996; Ulrich et al., 2012) and subducted sediments (e.g., Andres et al., 2002). However, it should be noted that: (1) the ocean crust is compositionally variably depleted and cannot be the enriched component (Niu and O'Hara, 2003; Niu et al., 2012); (2) if subducting slabs penetrate the 660 km discontinuity into the lower mantle, the subducted ocean crust would be ~2.5% denser than the ambient peridotitic mantle in the lower mantle conditions (Niu and O'Hara, 2003; Niu et al., 2012). Such huge negative buoyancy will impede the rise of the subducted crust to rise to the upper mantle MORB source regions; (3) if subducted terrigenous sediments were significant as an E-MORB source, such E-MORB would inherit their negative Nb-Ta anomalies (Plank and Langmuir, 1998), but these are not observed in the global MORB in general and in lavas from OH-1 and OH-3 segments in particular (Niu et al., 2001).

We thus emphasize that ancient subducted/recycled oceanic mantle lithosphere materials (both depleted melting residues and enriched metasomatic veins) may play the dominant role in causing the upper mantle heterogeneity as previously proposed (e.g., Niu et al., 2002). Niu and coauthors suggest that the basal portion of the growing oceanic lithosphere is enriched in metasomatic veins with elevated volatiles and incompatible elements due to the low-fraction (low-F) melt metasomatism (Niu and O'Hara, 2003; Niu et al., 2002; Niu and Green, 2018). These metasomatic veins would gradually accumulate radiogenic isotopes with the aging lithosphere. As such low-F melt metasomatism occurs continuously at the base of the growing lithosphere, we envision that recycling of these incompatible element-enriched metasomatic vein lithologies must have played an important role in generating enriched heterogeneities in the mantle since the beginning of plate tectonics. Partial melting of such highly enriched materials beneath the ridge would inevitably impart the elevated incompatible element abundances and high $^{87}Sr/^{86}Sr$, low ε_{Nd} and ε_{Hf} in the MORB melts, which is used effectively to explain the origin of compositionally highly variable seamount lavas flanking the East Pacific Rise (Niu et al., 2002; Zhang et al., 2016). More importantly, the subducted mantle lithosphere is less dense than the ambient mantle (Niu and O'Hara, 2003; Niu et al., 2012) and can thus return to the upper mantle source regions for E-MORB without requiring mantle plumes. In addition, the higher ε_{Hf} of the local depleted mantle defined by our OH-1 samples and other MAR 33–40°N basalts (Fig. 3), together with the recently identified highly radiogenic Hf isotopic compositions in in olivine-hosted melt inclusions of Azores basalts (Stracke et al., 2019), suggests the widespread presence of the very ancient depleted material in the Atlantic upper mantle, which is consistent with the explanation that recycled lithospheric mantle of ancient melting residues with the garnet signature may indeed act as the very depleted component.

5.2. Nature and origin of the OH-3 lavas mantle source

Although most OH-3 lavas are depleted in incompatible elements with $[La/Sm]_N < 1.0$ (except for OT11-10, OT11-12 and OT13-05 in blue doted circles in Fig. 5; also see Fig. S1), the OH-3 N-MORB samples also show variable Sr-Nd-Hf isotope compositions. It is obvious that Group-1 OH-3 samples plot overlapping with the most depleted OH-1 lavas in ε_{Hf}–$^{87}Sr/^{86}Sr$ and ε_{Hf}–ε_{Nd} spaces (Fig. 3). Therefore, the mantle source of these lavas is inferred to be dominantly (~97%) the depleted ADM mantle component as discussed above. In contrast, Group-2 OH-3 samples display decoupling between incompatible elements and the radiogenic isotopes, with low incompatible element concentrations, low $[La/Sm]_N$ but variably enriched Sr-Nd-Hf isotope characteristics (Fig. 5). Taken together, these Sr-Nd-Hf isotopic variations can also be explained as melting-induced mixing of two-component mantle that produced the OH-3 Group-2 N-MORB lavas. One endmember is the above mentioned ADM, and the other is an incompatible element depleted but isotopically variably enriched component, which can be termed as the enriched type II (E-type II; see Fig. 5 and Table 2).

The radiogenic Sr and unradiogenic Nd-Hf isotope characteristics of the Group-2 OH-3 lavas requires ancient evolution of an enriched component. However, it is clear as shown by chondrite normalized rare earth element patterns (Fig. S1) that these samples are more depleted in highly incompatible elements than in less incompatible elements, being consistent with an incompatible element depleted mantle source. Therefore, the observed decoupling in Group-2 samples (Figs. 3 and 5) requires that their ancient enriched mantle source must have experienced a melt extraction event in the recent past prior to the major melting event for the Group-2 MORB. This is also support by the evidence that the OH-2 Group-2 and three OH-1 samples deviate from the modelling trajectory in the $\alpha_{Sm/Nd}$ vs. $\alpha_{Lu/Hf}$ diagram (Fig. S2), which is consistent with the interpretation that simple one-stage melting model with anhydrous garnet lherzolite as a source material cannot account for the observed high $\alpha_{Sm/Nd}$ in these samples. Their high $\alpha_{Sm/Nd}$ (>0.95) is best explained as being caused by mantles source experienced melt extraction in recent past, which elevated Sm/Nd of the "residue" (future source). Partial melting of such a young mantle source with high Sm/Nd would produce magma with high Sm/Nd, i.e., high $[Sm/Nd]_{magma}$, but almost the same $^{143}Nd/^{144}Nd$.

In the context of the regional geology, the recent melting event nearby that could have produced the E-type II endmember, i.e., the signature of enriched isotopes and depleted incompatible elements, may be associated with the Azores mantle plume magmatism. This is because: (1) For on-axis plumes or off-axis plumes with a relatively short plume-ridge distance (<~500 km), the fertile plume materials could directly contribute to ridge magmatism, expressed as the E-MORB (for example, Iceland; Niu and Hékinian, 2004); (2) However, for a distal plume with

plume-ridge distances >1000 km, the along-ridge plume material flow undergoes continued decompression melting, making the flowing plume materials progressively depleted in the incompatible element and easily melted components, yet retaining the historically enriched isotopic signature (i.e., plume residues; Niu et al., 1999; Niu and Hékinian, 2004; Hall and Kincaid, 2004; Yang et al., 2017). Such "plume residues" contribute to the OH-3 Group 2 MORB. This scenario has been best exemplified by the occurrence of isotopically enriched N-MORB lavas in the Southwest Indian Ridge (Yang et al., 2017) and South Atlantic Ridge (Hanan et al., 1986; Fontignie and Schilling, 1996; Douglass et al., 1999). Spatially, Azores Triple Junction is about 1000 km north of the OH-3 segment, which is supposed to be the distal end of a plume. Temporally, magmatism associated with the Azores plume occurred less than 1.3 Ma (e.g., Hildenbrand et al., 2008). Therefore, the recent Azores plume melting residues may be a reasonable candidate that could provide such unique source material for the OH-3 magmatism. Furthermore, the Sr-Nd-Hf isotopic compositions of Azores mantle plume related lavas vary significantly (Elliott et al., 2007; Beier et al., 2007; Waters et al., 2020), indicating their melting residues must also be isotopically heterogenous. Therefore, it is expected that involvement of such isotopically varied compositions in the mantle source of mid-ocean ridge magmatism would inevitably contribute to the compositional diversity of MORB magmas, especially those incompatible element depleted N-MORB lavas. This complexity is illustrated in our calculation (Fig. 3 and Table S3) that the isotopic compositions of Group-2 OH-3 lavas can be produced by mixing between the 30–60% ADM and 70–40% Azores mantle plume residues of varying compositions (Elliott et al., 2007; Beier et al., 2007; Waters et al., 2020).

Note that mantle melting residues are likely refractory, but they are expected to re-melt to varying small extent as long as the conditions allow decompression. This has been well illustrated by secondary extension induced melting of the prior ridge melting residues in the Garrett transform in the Pacific (Wendt et al., 1999). While our interpretation of decompression melting of Azores plume residue beneath OH-3 seafloor spreading centers is reasonable, a further effort through a comprehensive study of MORB lavas from other magmatism starving segments, such as segment PO-7 and PO-8 (Detrick et al., 1995) in the north closer to Azores will help test this hypothesis.

5.3. Sr-Nd-Hf isotopic view on the distinct mantle sources of OH-1 and OH-3 lavas

On the basis of a comparative study on OH-1 and OH-3 MORB major and trace elements, Niu et al. (2001) conclude that OH-1 lavas are derived from an incompatible element/volatile enriched source with depressed solidus, resulting in greater extent of melting and thickened magmatic crust and magmatically robust ridge morphology and tomography. In contrast, OH-3 lavas are considered to be derived from an incompatible element/volatile depleted and more refractory source with low extent of melting, producing a thin crust and magmatically starved ridge morphology and topography. They further advocate that mantle source compositional variation controls the extent of mantle melting, crust production, gravity anomaly, ridge morphology and ridge segmentation at slow-spreading ridges like MAR.

Our new study fully supports this understanding, and also offers insights into the nature and origin of the varying enriched and depleted mantle source components in great fidelity by using Sr-Nd-Hf isotopes in combination with the existing major and trace element compositions of these basalts (Niu et al., 2001). The correlated variations of isotopes and incompatible element abundances and ratios defined by the majority of the OH-1 E-MORB samples (Fig. 5) is readily understood as resulting from partial melting of heterogeneous mantle developed in Earth's history with E-type I component lithologies dispersed in the more depleted ADM matrix. That is, the E-type I lithologies must have elevated abundances of incompatible elements, high $^{87}Sr/^{86}Sr$ but lower ε_{Nd} and ε_{Hf} relative to the depleted ADM matrix. Larger contribution of such E-type I component in the mantle source results in a more enriched signature in the melts. The good correlation between Sr-Nd-Hf isotopes and highly incompatible elements and heavy rear earth elements (Fig. 6) provide further evidence that the highly enriched E-type I component developed its incompatible element and isotope systematics in the garnet peridotite stability field. In contrast, the OH-3 N-MORB samples are best understood as partial melting of heterogenous mantle source dominated by incompatible element depleted ADM matrix that contains E-type II component with the signature of enriched isotopes but depleted incompatible elements as the result of a recent melt extraction event. This is also consistent with the poor correlations (or decoupling) between Sr-Nd-Hf isotopes and incompatible elements (Fig. 6).

The limited number of samples depleted in incompatible elements but enriched in Sr-Nd-Hf isotopes (OT16-11, OT18-11 and OT19-04; Fig. 5) indicates that the E-type II components also exist in the OH-1 mantle. Likewise, limited E-type I lithologies must also exist in the OH-3 mantle as indicated by three OH-3 E-MORB samples with $[La/Sm]_N > 1$ (Fig. 5). With all these observation considered, we conclude that OH-1 mantle includes an depleted component (i.e., ADM, characterized by low $[La/Sm]_N$, low $^{87}Sr/^{86}Sr$, high ε_{Nd} and extraordinarily high ε_{Hf}), an ancient enriched component (i.e., E-type I characterized by high $[La/Sm]_N$, high $^{87}Sr/^{86}Sr$, low ε_{Nd} and ε_{Hf}) and an incompatible element depleted but high $^{87}Sr/^{86}Sr$, low ε_{Nd} and ε_{Hf} E-type II component in limited abundance. In contrast, OH-3 mantle is dominated by the incompatible element depleted ADM and E-type II (characterized by low $[La/Sm]_N$ and variably enriched Sr-Nd-Hf isotopes) with minor presence of E-type I components. To better characterize the three mantle components, we summarize their nature and origin in Table 2. We suggest that the ADM may represent the regional mantle matrix beneath the Mid-Atlantic ridge, the E-type I and E-type II components are inferred to be compositional anomalous lithologies dispersed in the mantle matrix.

A schematic model (Fig. 7) is presented on the basis of elemental (Tables S1 and S2; Niu et al., 2001) and isotopic data to better illustrate the differences between OH-1 and OH-3 magmatic systems. In this cartoon, OH-1 mantle contains abundant (2–9%) E-type I component with a low solidus temperature (Fig. 7a; after Sanfilippo et al., 2019),

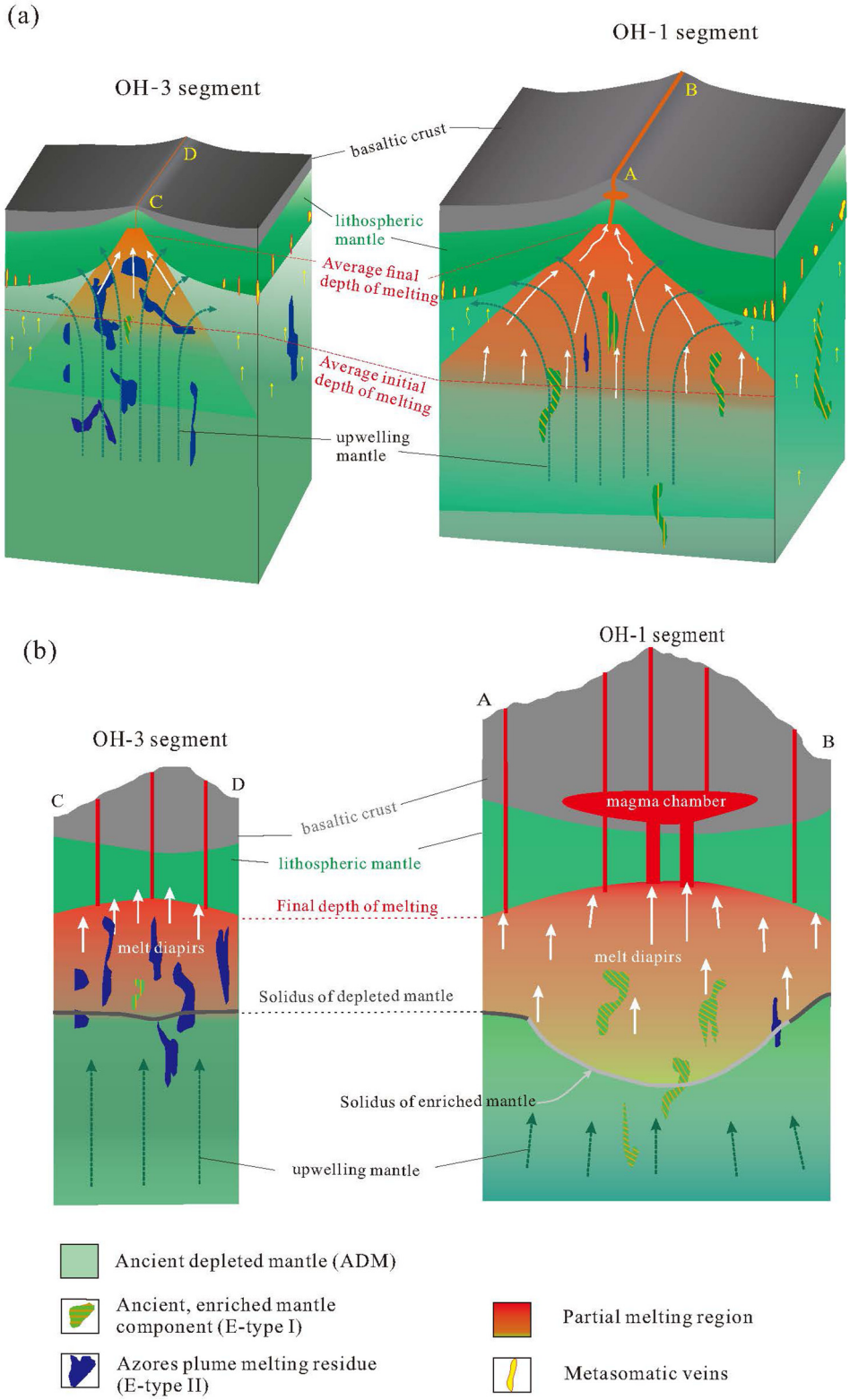

begins to melt deeper, has a greater melting interval, and melts to a larger extent than the more refractory OH-3 mantle. Therefore, OH-1 segment has thicker and more basaltic crustal mass. In contrast, the OH-3 mantle, dominated by incompatible element depleted ADM and E-type II components, is more refractory with high solidus temperature, begins to melt at a shallower depth with a lesser extent of melting, and thus producing a magmatically starved ridge segment with thinner crust (Fig. 7a). Fig. 7b (after Niu et al., 2001) illustrates the along-axis perspective for OH-1 and OH-3 segments, in which the magmatic accretion along the two segments ridge is the result of focused mantle upwelling and melting initiated by Rayleigh-Taylor gravitational instability developed in the partial melt zone (e.g., Whitehead et al., 1984). In detail, upwelling of a mantle domain containing abundant incompatible element and Sr-Nd-Hf isotopically enriched E-type I lithologies has resulted in a large decompression partial melting system that produces greater extent of melting, a steady-state magma chamber, thickened magmatic crust and a magmatically robust ridge morphology and tomography in the OH-1 segment. Because E-type I component abundance determines the initial depth of mantle melting of the focused upwelling system, it is expected that the produced magmas characterized by higher incompatible element abundances, higher $^{87}Sr/^{86}Sr$, lower ε_{Hf} and lower ε_{Hf} would occupy the segment center as is observed in Fig. 4 and in Niu et al. (2001). In contrast, upwelling of a lithological domain incorporating incompatible element depleted ADM and E-type II to a shallower level in the OH-3 mantle has led only to a small and weak magmatic system, which results in a less extent of melting, thinner magmatic crust, and a magmatically starved ridge morphology and tomography (Fig. 7b).

Note that the magmatism on the OH-1 segment is robust (Bideau et al., 1998; Niu et al., 2001) and there is an inferred magma chamber beneath the ridge (Niu et al., 2001) as evidenced by a seismic anomaly at depth of 3–5 km beneath a seamount near axis (Barclay et al., 1998). In this case, processes such as magma chamber mixing in the crust and melt aggregation in the mantle would potentially erase the specific characteristics of above-mentioned mantle components (i.e., E-type I, E-type II, ADM) to some extent, and the observed geochemical variations in OH-1 samples would actually represent the incomplete mixture. Therefore, the Sr-Nd-Hf isotopic composition of the MORB mantle source is speculated to be far more varied than shown in the MORB samples.

6. CONCLUSIONS

We identify three mantle components beneath the mid-Atlantic ridge 33–35°N using integrated elemental (Niu et al., 2001) and Sr-Nd-Hf isotopic data in this study. These include a depleted mantle with high radiogenic Hf isotope (ADM), an ancient enriched component (E-type I), and an incompatible element depleted but isotopically enriched component (E-type II). The ADM and E-type I most probably represent the recycled ancient depleted residual peridotite and the ancient metasomatic vein lithologies of the oceanic lithosphere, respectively, and the E-type II is explained as the melting residue of the Azores mantle plume with caveats. While the ADM may represent the regional mantle matrix beneath the Mid-Atlantic ridge, the E-type I and E-type II components are inferred to be physically distinct lithologies dispersed in the depleted mantle matrix. The OH-1 mantle source is mainly composed of the ADM matrix and E-type I material with limited E-type II component, whereas OH-3 mantle source primarily comprises the ADM and E-type II components with minor E-type I components. Such a Sr-Nd-Hf isotopic study on these MORB lavas provide further evidence to support the proposal in Niu et al. (2001) that mantle source heterogeneity exerts the dominant control on the contrasting differences in ocean crust thickness, mantle Bouguer anomalies, ridge tomography and morphology between OH-1 and OH-3 segments. That is, the MORB mantle source compositional variation exerts fundamentally important control on physical processes beneath and along ocean ridges (Niu et al., 2001; Niu, 2016).

Declaration of Competing Interest

The authors declare that they have no known competing financial interests or personal relationships that could have appeared to influence the work reported in this paper.

ACKNOWLEDGEMENT

This work was supported by NSFC grants (41776067, 41630968, 91958215), the NSFC-Shandong Joint Fund for Marine Science Research Centers (U1606401) and the 111 Project (B18048). PY thanks Jiliang Wang for assisting in drawing the

Fig. 7. Cartoons showing snapshots of our perceived mantle melting and melt extraction both across and along ridge axis beneath the MAR at OH-1 and OH-3, respectively. (a) Cross section of the OH-1 and OH-3 mantle across-axis (modified from Sanfilippo et al., 2019) to illustrate that varying amount of ancient enriched mantle components (E-type I, striped green patches) and substantial Azores-type mantle plume melting residual materials (E-type II, blue colored) are distributed in the depleted mantle matrix (ADM, light green colored), respectively. The OH-1 mantle source has more E-type I component with very limited E-type II components, whereas the mantle source of OH-3 lavas is dominantly the incompatible element depleted ADM and E-type II component with minor E-type I material. The different average solidi, as a function of the presence and relative abundance of the E-type I component in the mantle matrix, are also indicated with red dashed lines, defining the different melting regimes, melting volumes and decompression intervals. (b) Along-axis cross-sections (modified from Niu et al, 2001) to show the differences in ridge morphology, inferred crustal structure, mantle source lithology and melting regimes as explained in (a) above. Partial melting of the OH-1 mantle with more enriched E-type I components and greater decompression interval produces more melt to form thicker magmatic crust with a crustal magma chamber beneath the segment. Partial melting of the incompatible element depleted ADM and E-type II mantle components with short decompression interval produces less melt and thinner crust beneath OH-3 segment.

tomography map. The constructive and insightful comments by Vincent Salters, Lynne Elkins and two anonymous reviewers significantly improved the presentation and clarity of this manuscript. Finally, we also would like to thank Janne Blichert-Toft for editorial handling.

APPENDIX A. SUPPLEMENTARY MATERIAL

Supplementary data to this article can be found online at https://doi.org/10.1016/j.gca.2021.05.033.

REFERENCES

Andres M., Blichert-Toft J. and Schilling J. G. (2002) Hafnium isotopes in basalts from the southern Mid-Atlantic Ridge from 40° S to 55° S: Discovery and Shona plume–ridge interactions and the role of recycled sediments. *Geochem. Geophys. Geosyst.* **3**(10), 1–25.

Barclay A. H., Toomey D. R. and Solomon S. C. (1998) Seismic structure and crustal magmatism at the Mid-Atlantic Ridge, 35° N. *J. Geophys. Res. Solid Earth* **103**(B8), 17827–17844.

Beier C., Stracke A. and Haase K. M. (2007) The peculiar geochemical signatures of São Miguel (Azores) lavas: Metasomatised or recycled mantle sources?. *Earth Planet. Sci. Lett.* **259**(1–2), 186–199.

Bideau D., Hékinian R., Sichler B., Gracia E., Bollinger C., Constantin M. and Guivel C. (1998) Contrasting volcanic-tectonic processes during the past 2 Ma on the Mid-Atlantic Ridge: submersible mapping, petrological and magnetic results at lat. 34°52′N and 33°55′N. *Mar. Geophys. Res.* **20**(5), 425–458.

Blichert-Toft J. and Albarede F. (1997) The Lu–Hf isotope geochemistry of chondrites and the evolution of the mantle–crust system. *Earth Planet. Sci. Lett.* **148**, 243–258.

Blichert-Toft J., Agranier A., Andres M., Kingsley R., Schilling J. G. and Albarède F. (2005) Geochemical segmentation of the Mid-Atlantic Ridge north of Iceland and ridge-hot spot interaction in the North Atlantic. *Geochem. Geophys. Geosyst.* **6**(1).

Castillo P. R., Natland J. H., Niu Y. and Lonsdale P. F. (1998) Sr, Nd and Pb isotopic variation along the Pacific-Antarctic risecrest, 53–57 S: implications for the composition and dynamics of the South Pacific upper mantle. *Earth Planet. Sci. Lett.* **154**(1–4), 109–125.

Chen S., Wang X., Niu Y., Sun P., Duan M., Xiao Y. and Xue Q. (2017) Simple and cost-effective methods for precise analysis of trace element abundances in geological materials with ICP-MS. *Sci. Bull.* **62**(4), 277–289.

Debaille V., Blichert-Toft J., Agranier A., Doucelance R., Schiano P. and Albarede F. (2006) Geochemical component relationships in MORB from the Mid-Atlantic Ridge, 22–35 N. *Earth Planet. Sci. Lett.* **241**(3–4), 844–862.

DeMets C., Gordon R. G., Argus D. F. and Stein S. (1995) Current plate motions. *Geophys. J. Int.* **101**(2), 425–478.

Detrick R. S., Needham H. D. and Renard V. (1995) Gravity anomalies and crustal thickness variations along the Mid-Atlantic Ridge between 33° N and 40° N. *J. Geophys. Res.: Solid Earth* **100**(B3), 3767–3787.

Donnelly K. E., Goldstein S. L., Langmuir C. H. and Spiegelman M. (2004) Origin of enriched ocean ridge basalts and implications for mantle dynamics. *Earth Planet. Sci. Lett.* **226**(3–4), 347–366.

Dosso L., Bougault H., Langmuir C., Bollinger C., Bonnier O. and Etoubleau J. (1999) The age and distribution of mantle heterogeneity along the Mid-Atlantic Ridge (31–41 N). *Earth Planet. Sci. Lett.* **170**(3), 269–286.

Douglass J., Schilling J. G. and Fontignie D. (1999) Plume-ridge interactions of the Discovery and Shona mantle plumes with the southern Mid-Atlantic Ridge (40°-55° S). *J. Geophys. Res. Solid Earth* **104**(B2), 2941–2962.

Elliott T., Blichert-Toft J., Heumann A., Koetsier G. and Forjaz V. (2007) The origin of enriched mantle beneath São Miguel, Azores. *Geochim. Cosmochim. Acta* **71**(1), 219–240.

Fontignie D. and Schilling J. G. (1996) Mantle heterogeneities beneath the South Atlantic: a Nd-Sr-Pb isotope study along the Mid-Atlantic Ridge (3° S–46° S). *Earth Planet. Sci. Lett.* **142**(1–2), 209–221.

Gràcia E., Bideau D., Hekinian R. and Lagabrielle Y. (1999) Detailed geological mapping of two contrasting second-order segments of the Mid-Atlantic Ridge between Oceanographer and Hayes fracture zones (33° 30′ N-35° N). *J. Geophys. Res. Solid Earth* **104**(B10), 22903–22921.

Hanan B. B., Kingsley R. H. and Schilling J. G. (1986) Pb isotope evidence in the South Atlantic for migrating ridge-hotspot interactions. *Nature* **322**, 137–144.

Hall P. S. and Kincaid C. (2004) Melting, dehydration, and the geochemistry of off-axis plume-ridge interaction. *Geochem. Geophys. Geosyst.* **5**(12).

Hamelin C., Bezos A., Dosso L., Escartin J., Cannat M. and Mevel C. (2013) Atypically depleted upper mantle component revealed by Hf isotopes at Lucky Strike segment. *Chem. Geol.* **341**, 128–139.

Hildenbrand A., Madureira P., Marques F. O., Cruz I., Henry B. and Silva P. (2008) Multi-stage evolution of a sub-aerial volcanic ridge over the last 1.3 Myr: S. Jorge Island, Azores Triple Junction. *Earth Planet. Sci. Lett.* **273**(3–4), 289–298.

Hirschmann M. M. and Stolper E. M. (1996) A possible role for garnet pyroxenite in the origin of the "garnet signature" in MORB. *Contrib. Miner. Petrol.* **124**(2), 185–208.

Jacobsen S. B. and Wasserburg G. J. (1980) Sm–Nd isotopic evolution of chondrites. *Earth Planet. Sci. Lett.* **50**, 139–155.

Koornneef J. M., Stracke A., Bourdon B., Meier M. A., Jochum K. P., Stoll B. and Gronvold K. (2012) Melting of a two-component source beneath Iceland. *J. Petrol.* **53**(1), 127–157.

Le Roux P. J., Le Roex A. P., Schilling J. G., Shimizu N., Perkins W. W. and Pearce N. J. G. (2002) Mantle heterogeneity beneath the southern Mid-Atlantic Ridge: trace element evidence for contamination of ambient asthenospheric mantle. *Earth Planet. Sci. Lett.* **203**(1), 479–498.

Mahoney J. J., Sinton J. M., Kurz D. M., Macdougall J. D., Spencer K. J. and Lugmair G. W. (1994) Isotope and trace element characteristics of a super-fast spreading ridge: East Pacific Rise, 13–23°S. *Earth Planet. Sci. Lett.* **121**, 173–193.

Niu Y. (2016) The meaning of global ocean ridge basalt major element compositions. *J. Petrol.* **57**(11–12), 2081–2103.

Niu Y. L., Bideau D., Hekinian R. and Batiza R. (2001) Mantle compositional control on the extent of melting, crust production, gravity anomaly and ridge morphology: a case study at the Mid-Atlantic Ridge 33–35°N. *Earth Planet. Sci. Lett.* **186**, 383–399.

Niu Y. L., Regelous M., Wendt J. I., Batiza R. and O'Hara M. J. (2002) Geochemistry of near-EPR seamounts: Importance of source vs. process and the origin of enriched mantle component. *Earth Planet. Sci. Lett.* **199**, 329–348.

Niu Y. L., Wilson M., Humphreys E. R. and O'Hara M. J. (2012) A trace element perspective on the source of ocean island basalts (OIB) and fate of subducted ocean crust (SOC) and mantle lithosphere (SML). *Episodes* **35**(2), 310–327.

Niu Y. L. and O'Hara M. J. (2003) Origin of ocean island basalts: A new perspective from petrology, geochemistry and mineral physics considerations. *J. Geophys. Res.* **108**, 2209.

Niu Y. L., Collerson K. D., Batiza R., Wendt I. and Regelous M. (1999) The origin of E-type MORB at ridges far from mantle plumes: The East Pacific Rise at 11°20'N. *J. Geophys. Res.* **104**, 7067–7087.

Niu Y. L. and Green D. H. (2018) The petrological control on the lithosphere-asthenosphere boundary (LAB) beneath ocean basins. *Earth Sci. Rev.* **185**, 301–307.

Niu Y. L. and Hékinian R. (2004) Ridge suction drives plume-ridge interactions. In *Oceanic Hotspots*. Springer, Berlin, Heidelberg, pp. 285–307.

Niu Y. L., Waggoner D. G., Sinton J. M. and Mahoney J. J. (1996) Mantle source heterogeneity and melting processes beneath seafloor spreading centers: the East Pacific Rise, 18–19 S. *J. Geophys. Res. Solid Earth* **101**(B12), 27711–27733.

Paulick H., Münker C. and Schuth S. (2010) The influence of small-scale mantle heterogeneities on mid-ocean ridge volcanism: Evidence from the southern mid-Atlantic Ridge (7°30′S to 11°30′S) and Ascension Island. *Earth Planet. Sci. Lett.* **296**, 299–310.

Plank T. and Langmuir C. H. (1998) The chemical composition of subducting sediment and its consequences for the crust and mantle. *Chem. Geol.* **145**, 325–394.

Salters V. J. M., Mallick S., Hart S. R., Langmuir C. H. and Stracke A. (2011) Domains of de-pleted mantle, new evidence from hafnium and neodymium isotopes. *Geochem. Geophys. Geosyst.* **12**. doi.10.1029/2011GC003617.

Salters V. J. and Stracke A. (2004) Composition of the depleted mantle. *Geochem. Geophys. Geosyst.* **5**(5).

Sanfilippo A., Salters V., Tribuzio R. and Zanetti A. (2019) Role of ancient, ultra-depleted mantle in Mid-Ocean-Ridge magmatism. *Earth Planet. Sci. Lett.* **511**, 89–98.

Schilling J. G. (1975) Azores mantle blob: rare-earth evidence. *Earth Planet. Sci. Lett.* **25**(2), 103–115.

Schilling J. G., Zajac M., Evans R., Johnston T., White W., Devine J. D. and Kingsley R. (1983) Petrologic and geochemical variations along the Mid-Atlantic Ridge from 29 degrees N to 73 degrees N. *Am. J. Sci.* **283**(6), 510–586.

Shirey S. B., Bender J. F. and Langmuir C. H. (1987) Three-component isotopic heterogeneity near the Oceanographer transform, Mid-Atlantic Ridge. *Nature* **325**(6101), 217.

Stracke A., Genske F., Berndt J. and Koornneef J. M. (2019) Ubiquitous ultra-depleted domains in Earth's mantle. *Nat. Geosci.* **12**(10), 851–855.

Sun P., Niu Y., Guo P., Chen S., Duan M., Gong H. and Xiao Y. (2019) Multiple mantle metasomatism beneath the Leizhou Peninsula, South China: evidence from elemental and Sr-Nd-Pb-Hf isotope geochemistry of the late Cenozoic volcanic rocks. *Int. Geol. Rev.* **61**(14), 1768–1785.

Sun S.-S. and McDonough W. F. (1989) Chemical and isotope systematics of oceanic basalts: Implications for mantle composition and processes, in Magmatism in the Ocean Basins, edited by A. D. Saunders and M. J. Norry. *Geol. Soc. Spec. Publ.* **42**, 313–345.

Sun S. S. and Hanson G. N. (1975) Origin of Ross Island basanitoids and limitations upon the heterogeneity of mantle sources for alkali basalts and nephelinites. *Contrib. Miner. Petrol.* **52**(2), 77–106.

Ulrich M., Hémond C., Nonnotte P. and Jochum K. P. (2012) OIB/seamount recycling as a possible process for E-MORB genesis. *Geochem. Geophys. Geosyst.* **13**(6).

Van Orman J. A., Grove T. L., Shimizu N. and Layne G. D. (2002) Rare earth element diffusion in a natural pyrope single crystal at 2.8 GPa. *Contrib. Mineral. Petrol.* **142**(4), 416–424.

Waters C. L., Day J. M. D., Watanabe S., Sayit K., Zanon V., Olson K. M. and Widom E. (2020) Sulfide mantle source heterogeneity recorded in basaltic lavas from the Azores. *Geochim. Cosmochim. Acta* **268**, 422–445.

Waters C. L., Sims K. W. W., Perfit M. R., Blichert-Toft J. and Blusztajn J. (2011) Perspective on the genesis of E-MORB from chemical and isotopic heterogeneity at 9–10°N East Pacific Rise. *J. Petrol.* **52**, 565–602.

Wendt J. I., Regelous M., Niu Y., Hékinian R. and Collerson K. D. (1999) Geochemistry of lavas from the Garrett Transform Fault: insights into mantle heterogeneity beneath the eastern Pacific. *Earth Planet. Sci. Lett.* **173**, 271–284.

Whitehead J. A., Dick H. J. B. and Schouten H. (1984) A mechanism for magmatic accretion under spreading centers. *Nature* **312**, 146–147.

Yang A. Y., Zhao T. P., Zhou M. F. and Deng X. G. (2017) Isotopically enriched N-MORB: A new geochemical signature of off-axis plume-ridge interaction—A case study at 50° 28′ E, Southwest Indian Ridge. *J. Geophys. Res. Solid Earth* **122**(1), 191–213.

Zhang Y., Meng F. and Niu Y. (2016) Hf isotope systematics of seamounts near the East Pacific Rise (EPR) and geodynamic implications. *Lithos* **262**, 107–119.

Zindler A., Staudigel H. and Batiza R. (1984) Isotope and trace element geochemistry of young Pacific seamounts: implications for the scale of upper mantle heterogeneity. *Earth Planet. Sci. Lett.* **70**(2), 175–195.

Associate editor: Janne Blichert-Toft